Supplement of Biogeosciences, 21, 893–909, 2024
https://doi.org/10.5194/bg-21-893-2024-supplement

Biogeosciences
Open Access

Supplement of

Understanding the effects of revegetated shrubs on fluxes of energy, water, and gross primary productivity in a desert steppe ecosystem using the STEMMUS–SCOPE model

Enting Tang et al.

Correspondence to: Yijian Zeng (y.zeng@utwente.nl), Lingtong Du (dult80@nxu.edu.cn), and Zhongbo Su (z.su@utwente.nl)

1 Model Description

1.1 Energy fluxes

The SCOPE model constructs the surface energy balance by minimizing the energy balance closure error. The soil surface temperature and leaf temperature of all the layers are iterated until net radiation becomes equal to heat fluxes.

$$e_{bal} = R_n - LE - H - G \tag{S1}$$

where the net radiation (R_n) in SCOPE is computed by RTMo and RTMt sub-modules, calculating the incident radiation and thermal radiation emitted by the vegetation and soil, respectively. Incoming shortwave and longwave radiation are the main drivers for the RTMo module.

The latent heat flux (LE) describes the transfer of heat resulting from water phase changes, such as evaporation or transpiration. It is calculated as Eq.(S2) for leaf and soil elements, respectively:

$$LE = \lambda \frac{q_i - q_a}{r_a + r_s} \tag{S2}$$

where λ is the vaporization heat of water [J kg^{-1}]. q_i is the specific humidity in stomata or soil pores [kg m^{-3}]. q_a is the specific humidity above the canopy [kg m^{-3}]. r_a is aerodynamic resistance [s m^{-1}], a function of wind speed, canopy height and reference height calculated based on a two-source model (Wallace and Verhoef, 2000). r_s is stomatal resistance (r_{sc}) or soil surface resistance (r_{ss}) [s m^{-1}]. Within the iteration of the energy balance module, the aerodynamic and stomatal resistances are also updated because the atmospheric stability and vegetation photosynthesis are influenced by leaf temperatures.

$$r_{ss} = \exp\left(aa + bb - \mathrm{aa} \cdot \frac{\theta - \theta_r}{\theta_f - \theta_r}\right) \tag{S3}$$

$$r_{sc} = \frac{1}{g_s} = \frac{C_s - C_i}{1.6 \times A_n} \frac{\rho_a}{M_a} \frac{10^{12}}{p} \tag{S4}$$

where aa and bb are user-defined coefficients. θ is the volumetric soil water content [m^3 m^{-3}]. θ_r is the residual water content [m^3 m^{-3}]. θ_f is the field capacity [m^3 m^{-3}]. g_s is the stomatal conductance, which is defined as the inverse of r_{sc}. A_n is the net photosynthesis rate [μmol m^{-2} s^{-1}]. C_s and C_i is the boundary layer and internal CO_2 concentration [μmol m^{-3}], respectively. ρ_a is the specific mass of air [1.2047 kg m^{-3}]. M_a is the molecular mass of dry air [28.96 g mol^{-1}]. p is atmospheric pressure [hPa]. A detailed description of the calculations for A_n, C_s, C_i is given in Section 1.3.

Heat transferred via conduction between the surface and the atmosphere without state changes is defined as the sensible heat flux (H), which is calculated as (Troufleau et al., 1997):

$$H = \rho_a c_p \frac{T_s - T_a}{r_a} \tag{S5}$$

where ρ_a is the air density [1.2047 kg m^{-3}]. c_p is the specific heat of dry air [1004 J kg^{-1} K^{-1}]. T_s and T_a are the surface and air temperature [°C], respectively.

The ground heat flux (G) is calculated by the thermal diffusion equation, which estimates the G from the integrated time difference for a discrete time series of temperatures (Bennett et al., 2008):

$$G(t) = \frac{\Gamma}{\sqrt{\pi}} \int_{-\infty}^{t} \frac{dT(0,s)}{\sqrt{t-s}} \tag{S6}$$

where t is the current time step; $T(0,s)$ represents the skin temperature at soil surface (at depth zr = 0 cm) and s is the integration variable, supposing the skin temperature was simulated at discrete time $s_0, s_1, \dots, s_n$ over the period (t_{i-12}, t_i). Γ is the thermal inertia of the soil [J m^{-2} s$^{-1/2}$ K^{-1}], calculated as (Murray and Verhoef, 2007):

$$\Gamma = \sqrt{\lambda_s C_S} \tag{S7}$$

where C_S is the volumetric heat capacity of the soil [J m^{-3} K^{-1}] and λ_s is the heat conductivity of the soil [J m^{-1} s^{-1} K^{-1}]. C_s is parametrised from the two components in the soil:

$$C_S = \rho_s c_s (1 - \theta_s) + \rho_w c_w \theta \tag{S8}$$

where ρ_s is the soil bulk density [1.5 × 10^6 g m^{-3}]. c_s is the specific heat of the soil solids [0.83 J g^{-1} K^{-1}]. $\rho_w c_w$ is the heat capacity of water [4.2 × 10^6 J m^{-3} K^{-1}]. θ_s is the saturated soil moisture content [0.35 m^3 m^{-3}]. The thermal conductivity λ_s is a function of porosity [ε = 0.35 m^3 m^{-3}], sand and quartz fraction (similar to sand fraction, i.e., 0.7 in the study area).

Energy balance closure assessment

The energy balance closure issues in EC systems have been widely observed and studied, represented as the turbulent fluxes (i.e., LE+H) not always equal to the difference between available energy and ground heat flux (i.e., R_n- G) (Foken, 2008). Before assessing the closure of energy balance, the measured G at 10 cm depth (G_{10cm}) was calibrated to the ground heat flux G using calorimetric method (Gao et al., 2017):

$$G(t) = G_{zr}(t) + \sum_{I=1}^{I=i} C_{s,I}(t) \frac{\partial T_{s,\,I}}{\partial t} \delta Z_I \tag{S9}$$

where G_{zr} is the measured heat flux at a depth of zr (zr=10 cm). I is the number of sublayers (I=1). $C_{s,I}$ is the volumetric soil heat capacity for sublayer I (Eq. (S8)), where the θ becomes the average soil moisture of sublayer I. $\frac{\partial T_{s,\,I}}{\partial t}$ is the change in the soil temperature with time for sublayer I and the unit of t is seconds. δZ_I is the thickness of sublayer I (δZ_I=0.1 m). The soil temperature and moisture of sublayer I are the average of simulated surface temperature and soil moisture from STEMMUS–SCOPE and observed soil temperature and soil moisture at 10 cm depth, respectively. In this study, the observations of soil water content (SWC) and soil temperature (Ts) at 10 cm soil depth in 2016 and 2017 were absent, thereby the G_{10cm} was failed to convert to G. Therefore, only the energy fluxes in the growing season of 2018 and 2019 were valid for assessment.

The regression relation between (LE+H) and (Rn-G) has the slope (0.84) and intercept (19.11 W m^{-2}) in this site, which are superior to the average slope (0.67) and intercept (28.9 W m^{-2}) among eight EC sites of the ChinaFLUX network (Li et al., 2005). Thus, the energy balance closure adjustment has not been applied to observed LE and

H data but discarding the data greater than the closure threshold of $\pm$ 100 Wm^{-2} (Valayamkunnath et al., 2018). The closure threshold can be quantified as follows:

$$D = |(Rn - G) - (LE + H)| \tag{S10}$$

1.2 Water fluxes

With the simulated surface temperature as a boundary condition, STEMMUS model further simulates soil moisture and soil temperature under a two-phase mass and heat transfer mechanism. The governing equations are:

Soil water conservation equations

$$\frac{\partial}{\partial t}(\rho_L \theta_L + \rho_V \theta_V) = -\frac{\partial}{\partial z}(q_L + q_V) - S \tag{S11}$$

where ρ_L and ρ_V are the density of liquid water and water vapor [kg m^{-3}], respectively. θ_L and θ_V are the volumetric water content for liquid and water vapor [m^3 m^{-3}], respectively. z is the vertical space coordinate (positive upwards) [m]. S is the sink term for the root water extraction which is calculated in Root Water Uptake (RWU) module [cm s^{-1}]. q_L and q_V are the liquid water flux and the water vapor flux [kg m^{-2} s^{-1}], expressed by three components: isothermal flux (denoted by "h", thermal flux (denoted by "T") and advective flux (denoted by "a").

$$q_L = q_{Lh} + q_{LT} + q_{La} = -\rho_L \left[K_{Lh} \left(\frac{\partial h}{\partial z} + 1 \right) + (K_{LT} + D_{Ta}) \frac{\partial T_s}{\partial z} + \frac{K_{Lh}}{\gamma_w} \frac{\partial P_g}{\partial z} \right]$$

$$q_V = q_{Vh} + q_{VT} + q_{Va} = -(D_{Vh} \frac{\partial h}{\partial z} + D_{VT} \frac{\partial T_s}{\partial z} + D_{Va} \frac{\partial P_g}{\partial z}) \tag{S12}$$

K_{Lh} is the isothermal hydraulic conductivity [m s^{-1}] while K_{LT} is the thermal hydraulic conductivity [m^2 s^{-1} °C^{-1}]. h is the capillary pressure head [m]. T_s is the soil temperature [°C]. P_g is the mixed pore-air pressure [Pa]. γ_w is the specific weight of water [kg m^{-2} s^{-2}]. D_{Ta} is the transport coefficient for adsorbed liquid flow caused by the temperature gradient [m^2 s^{-1} °C^{-1}]. D_{Vh} is the isothermal vapor conductivity [kg m^{-2} s^{-1}]. D_{VT} is the thermal vapor diffusion coefficient [kg m^{-1} s^{-1} °C^{-1}]. D_{Va} is the advective vapor transfer coefficient [s] (Zeng et al., 2011b, a). Overall, the liquid water fluxes (i.e., q_{Lh}, q_{LT}, and q_{La}) and water vapor fluxes (i.e., q_{Vh}, q_{VT}, and q_{Va}) are driven by the gradient of matric potential, temperature, and air pressure, respectively (Wang et al., 2021).

Dry air transfer equations

STEMMUS model introduces the dry air transport mechanism using Henry's law to describe dissolved gases in soil water:

$$\frac{\partial}{\partial t}[\varepsilon \rho_{da}(S_a + H_c S_L)] = -\frac{\partial q_a}{\partial z} \tag{S13}$$

where ε (= 0.35 m^3 m^{-3}) is the porosity. ρ_{da} is the density of dry air [kg m^{-3}]. S_a (= 1-S_L) and S_L(= θ_L/ε) are the degree of air saturation and saturation in the soil, respectively. H_c (= 0.02) is Henry's constant. The dry air flow q_a [kg m^{-2} s^{-1}] is driven by the dry air concentration and air pressure gradient:

$$q_a = -(\underbrace{D_e \frac{\partial \rho_{da}}{\partial z}}_{\text{Diffusive flux}} + \underbrace{\rho_{da} K_g \frac{\partial P_g}{\partial z}}_{\text{Advective flux}} - \underbrace{H_c \rho_{da} \frac{q_L}{\rho_L}}_{\text{Dispersive flux}} + \underbrace{\theta_a D_{Vg} \frac{\partial \rho_{da}}{\partial z}}_{\text{Dissolved air}}) \tag{S14}$$

D_e is the molecular diffusivity of water vapour in soil [m^2 s^{-1}]. K_g is the intrinsic air permeability [m^2]. q_L is the liquid water flux [kg m^{-2} s^{-1}]. θ_a (=θ_V) is the volumetric fraction of dry air in the soil, and D_{Vg} is the gas-phase longitudinal dispersion coefficient [m^2 s^{-1}] (Zeng et al., 2011b, a).

Root Water Uptake

The equation to calculate root water uptake is as follows (Wang et al., 2021):

$$\sum_{i=1}^{n} \frac{\psi_{s,i} - \psi_l}{r_{s,i} + r_{r,i} + r_{x,i}} = \frac{0.622}{P} \frac{\rho_{da}}{\rho_V} \left(\frac{e_l - e_a}{r_c + r_a}\right) = T \tag{S15}$$

where $\psi_{s,i}$ and ψ_l are the water potential [m] for soil at ith layer and leaf, respectively. $r_{s,i}$ is the soil hydraulic resistance [s m^{-1}]. $r_{r,i}$ is the root resistance to water flow radially across the roots [s m^{-1}]. $r_{x,i}$ is the plant axial resistance to flow from the soil to leaves [s m^{-1}]. P is the atmospheric pressure [Pa]. 0.622 is the ratio of the molar mass of water to air. ρ_{da} and ρ_V are the density of dry air and water vapor [kg m^{-3}], respectively. e_l and e_a are the vapor pressure of leaf and atmosphere [hPa], respectively. r_a and r_c are the aerodynamic resistance and canopy resistance [s m^{-1}], respectively. T is the transpiration.

Evapotranspiration

The evapotranspiration (ET) is the sum of the evaporation and transpiration [mm 30-min^{-1}]. Evaporation and Transpiration are calculated from the latent heat fluxes of soil (LE_{stot}) and canopy (LE_{ctot}), respectively.

$$Transpiration = \frac{LE_{ctot}}{\lambda} \tag{S16}$$

$$Evaporation = \frac{LE_{stot}}{\lambda} \tag{S17}$$

where the λ is the latent heat of vaporization of liquid water [2.454×10^6 J m^{-3}].

1.3 Carbon fluxes

Gross primary productivity

The C3 Photosynthesis can be expressed as the minimum of two processes (Farquhar et al., 1980): (a) carboxylation rate limited by Ribulose biphosphate-carboxylase-oxygenase activity (i.e., enzyme-limited, V_c, described as Eq. (S18)) or (b) carboxylation rate limited by Ribulose 1-5 bisphosphate regeneration rate (i.e., electron transport/light -limited, V_e, described as Eq. (S19) (Bayat et al., 2019; Wang et al., 2021):

$$V_c = V_{cmax} \cdot \mathrm{WSF} \cdot \frac{C_i - \Gamma^*}{C_i + K_c(1 + \frac{O_i}{K_o})} \tag{S18}$$

$$V_e = \frac{J(C_i - \Gamma^*)}{5(C_i + 2\Gamma^*)} \tag{S19}$$

V_{cmax} is the maximum carboxylation rate [μmol m^{-2} s^{-1}]. WSF is the water stress factor calculated as Eqs. (S20) - (S21). C_i is the internal CO_2 concentration [μmol m^{-3}] and the first C_i is calculated by the equation $C_i = C_s(1 - \frac{1}{mRH})$ and the following C_i is obtained by iteration of Eq. (S26). $\Gamma^*$is the CO_2 compensation point in the absence of mitochondrial respiration. K_c and K_o are the Michaelis-Menten constants for carboxylation and oxygenation [μmol m^{-3}], respectively. O_i is the leaf internal oxygen concentration [μmol m^{-3}] and J is the electron transport rate [μmol m^{-2} s^{-1}].

$$WSF(i) = \frac{1}{1+e^{-100\theta_s(\theta(i)-\frac{\theta_f+\theta_r}{2})}} \cdot bbx \tag{S20}$$

$$WSF = \sum_{i=1}^{n} RF(i) \cdot WSF(i) \tag{S21}$$

where $WSF(i)$ is the WSF at i^{th} soil layer, determined by the soil hydraulic properties. bbx indicates whether the root exists. $RF(i)$ is the ratio of root length at i^{th} soil layer to total root length. In addition to the V_c and V_e, the key variables solved within the Farquhar model are described in Eqs. (S22) – (S24):

$$A_n = \min(V_c, V_e) = A_g - R_d \tag{S22}$$

$$R_d = Rdparam \cdot V_{cmax} \cdot \frac{e^{log_{1.8} \cdot q_t}}{1+e^{1.3\,(T-Trdm)}} \tag{S23}$$

$$C_s = C_a - \frac{(C_a - C_i)r_a}{r_a + r_s} \tag{S24}$$

where A_n and A_g are the net and gross photosynthesis [μmol m^{-2} s^{-1}], respectively. R_d is the dark respiration, calculated by multiplying its fraction of V_{cmax} ($Rdparam = 0.025$) with the temperature corrected V_{cmax}. $q_t = 0.1 * (T - Tref)$, where T is the temperature of leaf in shade and $Tref$ [K] is the absolute temperature at 25 °C; $Trdm$ is the temperature at which respiration is lower than half that predicted by the proportional change in respiration with a 10 °C increase in temperature (Q_{10} = 2). C_a and C_s are the CO_2 concentration in the atmosphere and boundary layer [μmol m^{-3}], respectively.

Based on the relationship between photosynthesis and g_s for H_2O and CO_2 diffusion (Eq. (S4) & Eq.(S26)), the Eqs. (S18) - (S24) of the Farquhar model and the Eq. (S25) of the Ball-Berry model are solved jointly to derive three unknown variables A_n, g_s and C_i :

$$g_s = \max\ (b,\ \mathrm{m}\ \frac{A_n \times RH}{C_s} + b) \tag{S25}$$

where the unit of g_s is [μmol m^{-2} s^{-1}]. m and b are the slope and intercept [unitless] of Ball-Berry stomatal conductance model (Collatz et al., 1991). RH is relative humidity at the leaf surface [%]. At each iteration, the internal CO_2 concentration is updated as Eq. (S26) based on the Fick's Law,

$$C_i = C_s - 1.6\ \frac{A_n}{g_s} \tag{S26}$$

where factor 1.6 accounts for conversion from conductance for H_2O to CO_2 diffusion.

1.4 Model input

The governing variables and critical parameters to drive the model are listed in Table S1, which are estimated based on local experts, literature and calibration performance (Jiang et al., 2021; Liang et al., 2021; Jackson et al., 1997; Lai et al., 2016; Abu-Hamdeh, 2003; Jia et al., 2018; Wei et al., 2019; Gong et al., 2016; Mwangi et al., 2020; Montzka et al., 2017). China Meteorological Forcing Dataset (CMFD) developed by He et al. (2020) was validated with available forcing data, further used as the supplementary data to fill the data gap in the forcing data.

Table S1. Governing variables and parameters for the STEMMUS–SCOPE model in Yanchi County, China.

Symbol	Variables	Unit	Value	
Half-hourly time series of meteorological forcings				
rainfall	Precipitation	[mm]		
T_a	Air temperature	[°C]		
RH	Relative humidity	[%]		
p	Atmospheric pressure [a]	[hPa]		
u	Wind speed [b]	[m s^{-1}]	Figure S1	
CO_2	Carbon dioxide concentration	[mg m^{-3}]		
R_{li}	Incoming longwave radiation	[W m^{-2}]		
R_{in}	Incoming shortwave radiation	[W m^{-2}]		
LAI	Leaf area index	[m^2 m^{-2}]		
e_a	Air vapor pressure	[hPa]	$e_a = \frac{e_s\,RH}{100} = 6.107 \times 10^{\frac{7.5\,T_a}{237.3+T_a}} \times \frac{RH}{100}$	
VPD	Vapor pressure deficit	[hPa]	$VPD = 6.107 \times 10^{\frac{7.5\,T_a}{237.3+T_a}}\ (1 - \frac{RH}{100})$	
T_{sur}	Soil surface temperature [c]	[°C]	Simulated by SCOPE model	
Canopy parameters		**Unit**	**C3 Shrub**	**C3 Grassland**
V_{cmax}	Maximum carboxylation rate	[μmol m^{-2} s^{-1}]	123	123
Ballberry0	Ball-Berry stomatal conductance	[-]	0.025	0.025
m	parameter	[-]	6.8	6.8
h_c	Canopy height	[m]	1.4	0.03
d	Leaf width	[m]	0.005	0.002
LIDFa	Leaf inclination	[-]	-0.33	-0.33
LIDFb	Variation in leaf inclination	[-]	-0.15	-0.15
Soil parameters and soil profiles		**Unit**	**C3 Shrub**	**C3 Grassland**
SWC	Initial soil water content	[m^3 m^{-3}]	Estimated based on in-situ measurement	
Ts	Initial soil temperature	[°C]	Table S2	
K_{sat}	Saturated hydraulic conductivity	[cm d^{-1}]	100	
ε	Porosity	[m^3 m^{-3}]	0.35	
θ_s	Saturated SWC	[m^3 m^{-3}]	0.35	
θ_r	Residual SWC	[m^3 m^{-3}]	0.014	
α	Van Genuchten parameters	[m^{-1}]	0.005	
n		[-]	1.71	
θ_f	Field capacity	[m^3 m^{-3}]	0.15	
ρ_s	Bulk density	[g cm^{-3}]	1.5	
c_s	Specific heat of sandy soil	[J g^{-1} K^{-1}]	0.83	
Root parameters		**Unit**	**C3 Shrub**	**C3 Grassland**
R_{depth}	Maximum Rooting depth	[cm]	269	30
β	Fitted extinction coefficient	-	0.9674	0.943
R_D	Biomass density	[gDM m^{-3}]	4.92×10^5	2.1×10^5
RTB	Initial root total biomass	[g m^{-2}]	1500	1000
r_{root}	Root radius	[mm]	0.5	0.2

[a] Boundary condition for dry air transportation in the soil.
[b] Wind speed data of 2019 was obtained from ERA5 dataset because CMFD is only available till year 2018.
[c] Boundary condition for heat transport.

Table S2. Initial soil profile for the simulation in 2018 (for calibration) and in 2016, 2017 and 2019 (for validation).

	2016 (DOY 122 – DOY 274)		2017 (DOY 121 – DOY 190)		2018 (DOY 121 – DOY 212)		2019 (DOY 122 – DOY 274)	
Depth	**Ts (°C)**	**SWC (m^3 m^{-3})**	**Ts (°C)**	**SWC (m^3 m^{-3})**	**Ts (°C)**	**SWC (m^3 m^{-3})**	**Ts (°C)**	**SWC (m^3 m^{-3})**
0 cm	20.5	0.046	20	0.046	17	0.046	15	0.08
10 cm	20.23	0.046	19.5	0.046	15.53	0.046	14.5	0.09
20 cm	20	0.046	18	0.046	13.34	0.046	14	0.09
50 cm	19	0.06	17	0.06	12.42	0.06	13.5	0.13
100 cm	16	0.12	15	0.12	11.98	0.12	12.5	0.12
150 cm	13	0.11	13	0.11	10.74	0.11	11.5	0.11
300 cm	10	0.1	10	0.1	9	0.1	10	0.1
500 cm (Bottom)	8.3	0.1	8.3	0.1	8.3	0.1	8.3	0.1

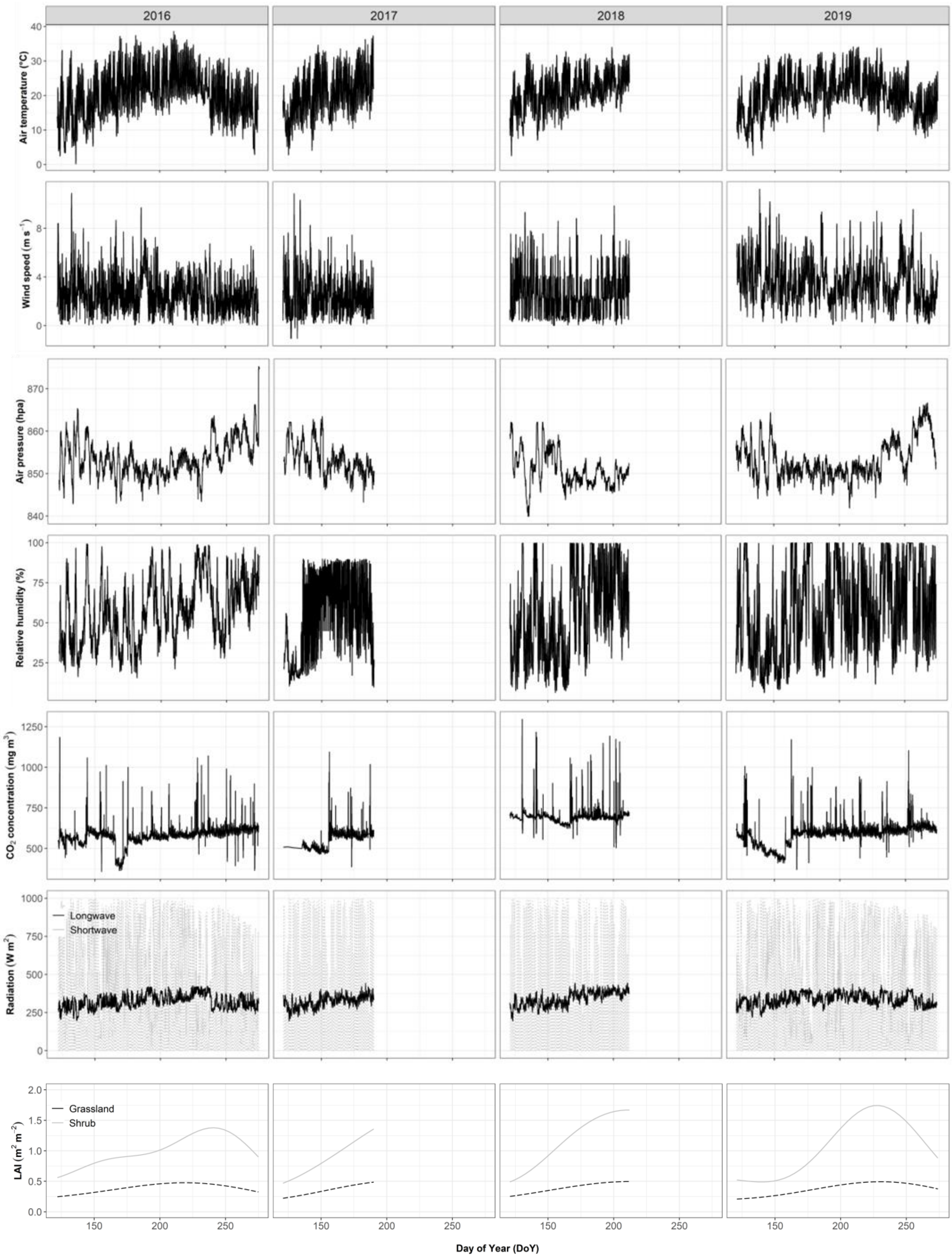

185

Figure S1. Input data for STEMMUS-SCOPE mode

2 Reconstructed LAI

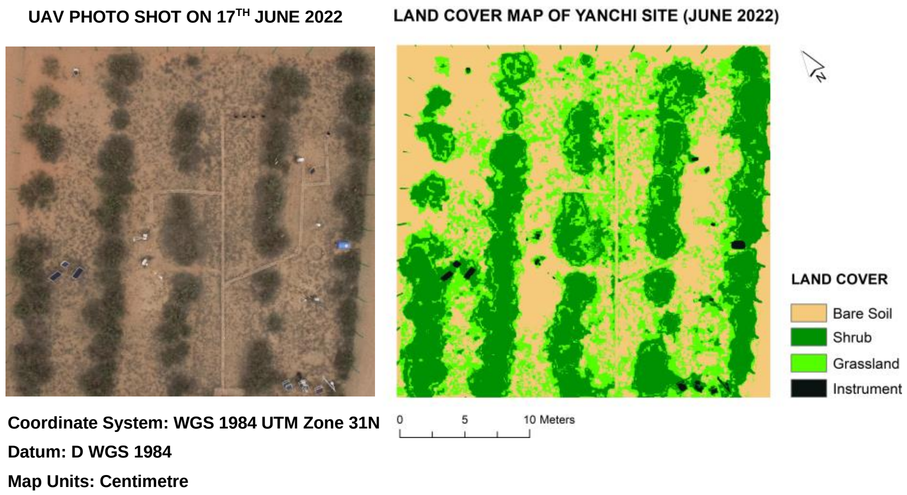

Figure S2. Land cover classification map.

Table S3. Fractional coverage of shrubs, grasses and bare soil and the approximated contributions from shrubs and grasses.

Land Cover	Number of pixels	Fractional coverage in field	Contribution in simulated fluxes*
Shrub	268,325,3	35 %	58.33 %
Grassland	195,308,4	25 %	41.67 %
Bare Soil	317,921,8	40 %	Implicitly included for either Shrub grid or Grass grid
Instrument	354,78	/	/

*This contribution will be further used to aggregate the simulated fluxes of the shrubs-grassland scenario (including contribution of bare soil evaporation).

Table S4. Parameters used in HANTS algorithm to smooth MODIS 4d LAI during 2016–2022 (Roerink et al., 2000; Abouali, 2012).

Parameters	Description	Shrub	Grass
ni	total number of samples	622	622
nb	the length of the base period	622	622
nf*	number of frequencies	30	15
ts	array of sample size	1:622	1:622
low	valid range minimum	0	0
high*	valid range maximum	2	0.5
fet	fit error tolerance	5	5
dod	degree of overdeterminedness	1	1
delta	small positive number (e.g. 0.1) to suppress high amplitudes	0.1	0.1

*To differentiate the LAI of different land covers, the curve-fitting process is mainly controlled by nf and high.

Table S5. Calculation of the actual LAI (LAI_a) for shrub in different years.

Year	Variable for Shrub	DOY 160.5	DOY 168.5
2022	LAI_{HANTS}_2022	0.21	0.20
	LAI_a_2022 (calculate from measured LAI_e) *	0.40	0.54
	ratio = $\frac{LAI_a\_2022}{LAI_{HANTS}\_2022}$	1.92	2.73
2019	LAI_{HANTS}_2019	0.25	0.29
	LAI_a_2019 = ratio * LAI_{HANTS}_2019	0.48	0.80
2018	LAI_{HANTS}_2018	0.48	0.55
	LAI_a_2018 = ratio * LAI_{HANTS}_2018	0.93	1.49
2017	LAI_{HANTS}_2017	0.40	0.45
	LAI_a_2017 = ratio * LAI_{HANTS}_2017	0.77	1.24
2016	LAI_{HANTS}_2016	0.37	0.38
	LAI_a_2016 = ratio * LAI_{HANTS}_2016	0.71	1.05

* LAI_e is the effective LAI measured by LAI-2200C (LAI-2200C, LI- COR Inc., USA). The LAI_e was converted into the LAI_a according to a fitting equation $LAI_e = 2.517\ LAI_a + 0.2245$ (Tang et al., 2014).

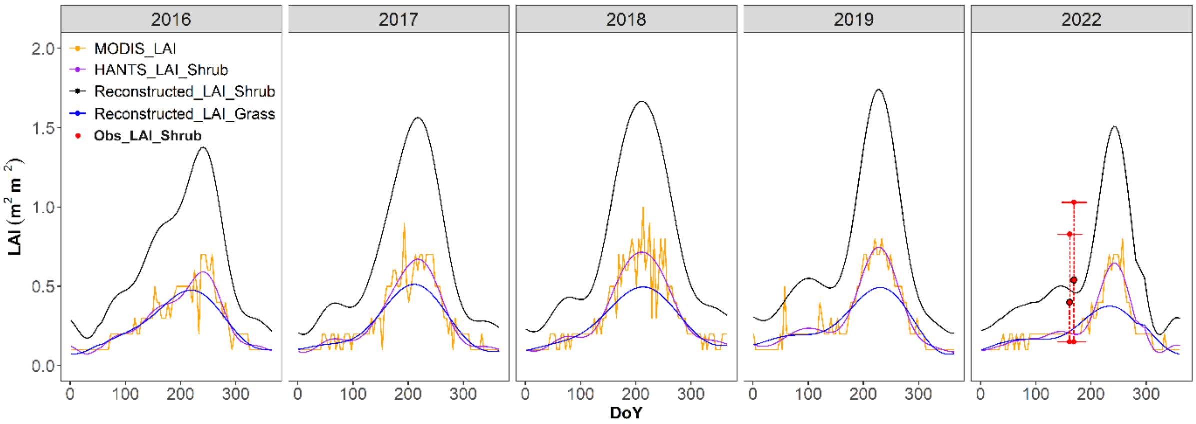

Figure S3. Reconstructed 4-day LAI for shrubs and grasses, respectively. HANTS_LAI_Shrub in purple represents the smoothed MODIS_LAI with the setting of nf=30 and high=2 in HANTS algorithm and then Reconstructed_LAI_Shrub in black is derived by multiplying HANTS_LAI_Shrub by 2.33. Reconstructed_LAI_Grass in blue is obtained by smoothing the MODIS_LAI with nf=15 and high=0.5 in HANTS algorithm. The red dots (Obs_LAI_Shrub) are the LAI_a calculated from LAI_e measured in June 2022 (Table S5), where the dotted lines represent the range of LAI_a.

3 Sensitivity analysis

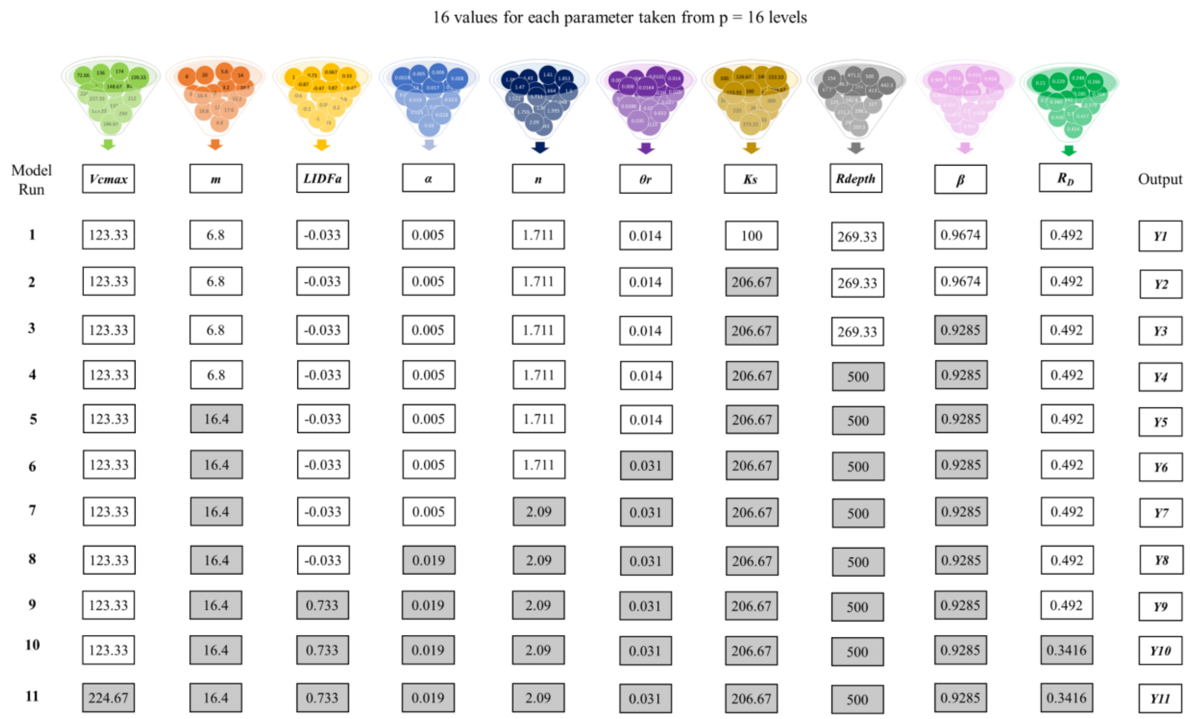

Figure S4. Sampling strategy of Morris method used in this study: an example of one of the trajectories (r = 20) from p^k (16^7) sampling space. Model run NO.1 is one of the parameters combinations randomly selected from 16^7 sampling space, as a starting point for a trajectory. Each trajectory includes eight model runs, which resulted in total 20 × 11 = 220 model runs in SA. Filled grids indicate the parameter values that was being modified.

As the start of Morris SA, we had a n-dimension p-level orthogonal input space and STEMMUS-SCOPE model Y = y(x_1, x_2, ….. x_n). Parameters are assumed to be uniformly distributed in [0,1] and randomly take values from {0, 1/(p-1), 2/(p-1), … , 1}. A trajectory Y(x_1,…, x_k) is then generated. The elementary effect (EE) of the i^{th} input is calculated as:

$$EE_i = \frac{Y(x_1,\ldots,x_{i-1},x_i+\Delta_i,x_{i+1},\ldots,x_k)-Y(x_1,\ldots,x_k)}{\Delta_i} \quad \text{(S27)}$$

where k is the number of parameters (k = 10) and p is the number of levels (p = 16). Δ is the variation in the parameter x_i, predetermined as the multiple of $1/(p-1)$. Each input parameter in a trajectory is assumed to vary across Δ, introducing $(k+1)$ elementary effects. Only one input parameter was perturbed between two successive runs of the model (Fig. S4). To achieve the stability of the SA results, r different trajectories ($r = 20$) were randomly sampled from the p^k (16^7) sampling space. Thus, the total runs of the model are $r(k+1)$. The output of Morris sensitivity analysis are: (i) μ^* for assessing the influence of a parameter on the simulations (Campolongo et al., 2007), (ii) σ for measuring the interactions between parameters (Morris, 1991).

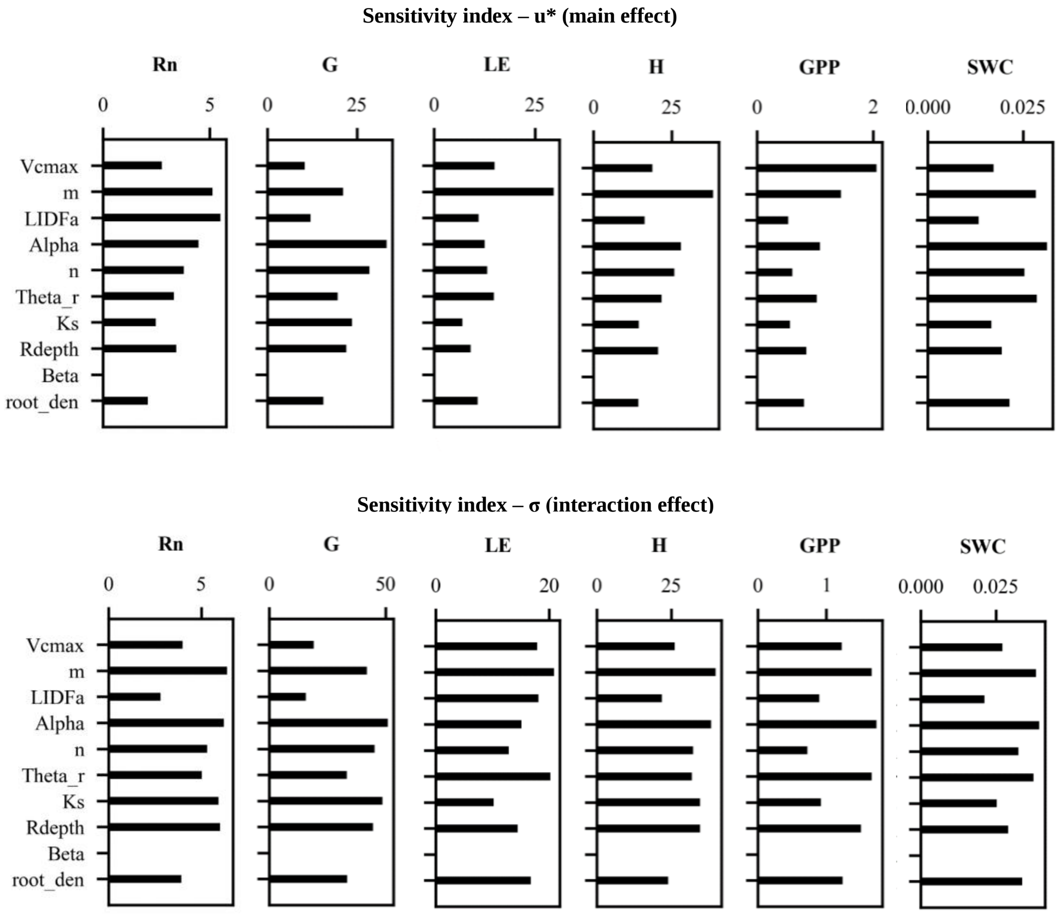

Figure S5. The sensitivity index of parameters to modelled net radiation (R_n), ground heat flux (G), latent heat flux (LE) and sensible heat flux (H), soil water content (SWC) and gross primary productivity (GPP) over May to July in 2018. Fitted extinction coefficient (β) displayed zero value for both main and interaction effects because Morris method is unable to capture significant effect due to the limited variation [0.909, 0.982] in the pre-defined parameter range.

4 Performance of model calibration

SWC and Soil Temperature

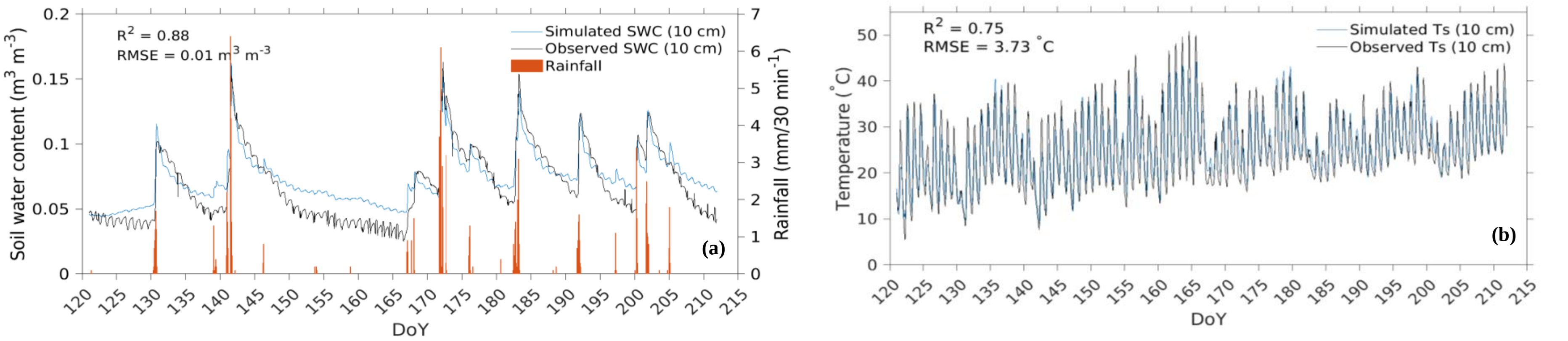

Figure S6. Temporal dynamics of simulated (a) soil water content (SWC) and (b) soil temperature (Ts) at 10 cm depth from grass grid modelling (i.e., grassland ecosystem) versus observed values during May–September in 2018.

Energy fluxes and GPP

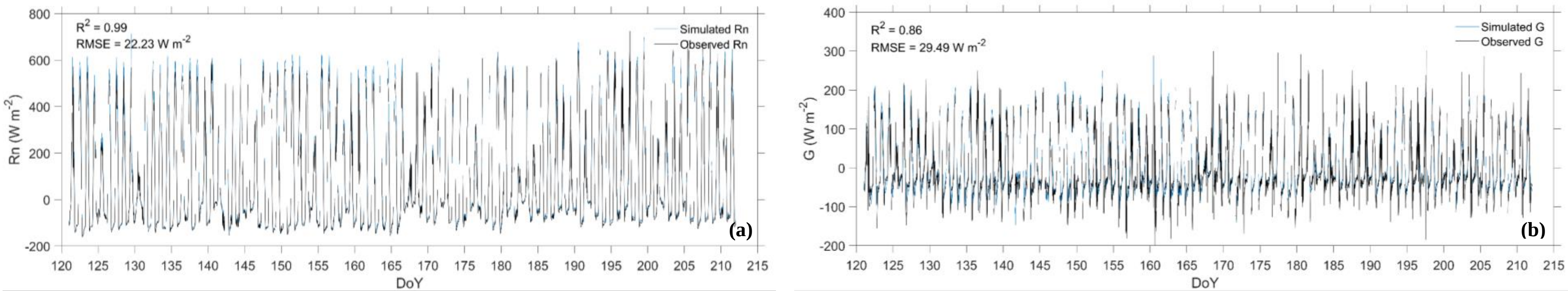

Figure S7. Temporal dynamics of composited (a) Net Radiation (R_n) and (b) Ground Heat Flux (G) that aggregated from simulated fluxes from shrub grid (58.33%) and grass grid (41.67%) (i.e., shrubs-grassland ecosystem) versus observations during May–July in 2018.

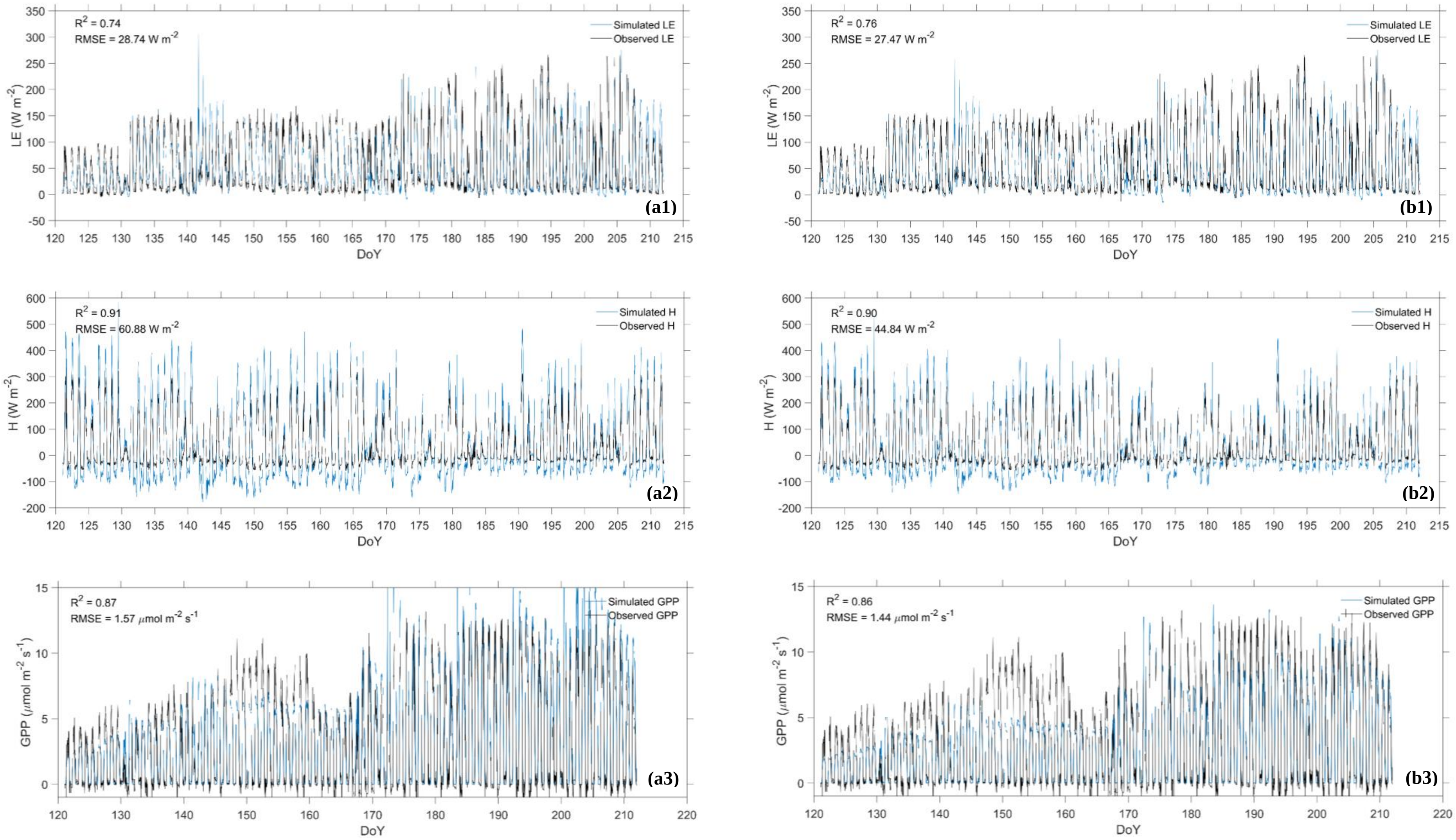

Figure S8. Comparison of simulated latent heat flux (LE), sensible heat flux (H) and gross primary productivity (GPP) from: (a) shrub grid modelling and (b) aggregated fluxes from both shrub grid and grass grid during May–July in 2018.

Table S6. Comparison of summary statistics between model validation (Val) and calibration (Cal).

	Period	Samples (n)	R^2	RMSE
SWC	Cal	4368	0.88	0.01 m^3 m^{-3}
	Val	7344	0.84	0.01 m^3 m^{-3}
Ts	Cal	4368	0.75	3.73 ℃
	Val	7344	0.85	2.74 ℃
$\boldsymbol{R_n}$	Cal	3908	0.99	22.23 W m^{-2}
	Val	16741	0.91	66.90 W m^{-2}
G	Cal	3908	0.86	29.49 W m^{-2}
	Val	6083	0.89	19.64 W m^{-2}
LE	Cal	3908	0.76	27.47 W m^{-2}
	Val	16741	0.67	33.94 W m^{-2}
H	Cal	3908	0.90	44.84 W m^{-2}
	Val	16741	0.76	59.63 W m^{-2}
GPP	Cal	3908	0.86	1.44 μmol m^{-2} s^{-1}
	Val	16741	0.70	1.73 μmol m^{-2} s^{-1}

5 Results

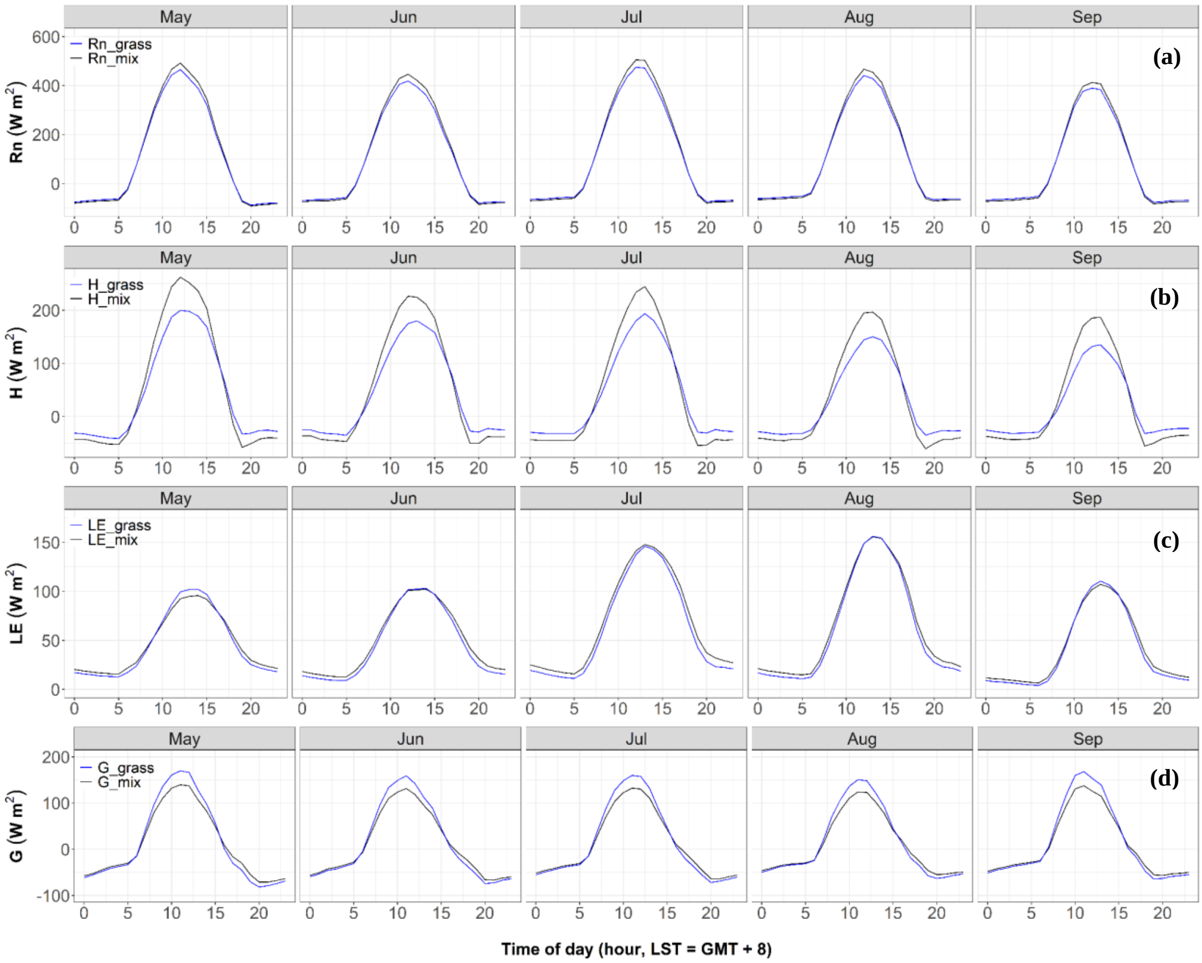

Figure S9. Diurnal courses of (a) net radiation (R_n), (b) sensible heat flux (H), (c) latent heat flux (LE) and (d) ground heat flux (G) during May–September in 2016 and 2019. Hereafter, the 'grass' in the legend denotes grassland ecosystem and 'mix' denotes shrubs-grassland ecosystem.

Table S7. Seasonal averaged value of simulated SWC under shrubland and grassland.

	Growing season in 2016		**Growing season in 2019**	
SWC unit: [m^3 m^{-3}]	Grassland	**Shrub**	Grassland	**Shrub**
Rainfall (Sum)	218.1 mm (*dry*)		292.4 mm (*normal*)	
10 cm SWC (Mean ± SD)	0.072 ± 0.018	0.063 ± 0.014	0.079 ± 0.018	0.075 ± 0.018
Difference (Shrub − Grassland)	− 0.009 ± 0.007		− 0.004 ± 0.006	
100 cm SWC (Mean ± SD)	0.084 ± 0.009	0.070 ± 0.009	0.089 ± 0.008	0.082 ± 0.011
Difference (Shrub − Grassland)	− 0.014 ± 0.007		− 0.008 ± 0.005	

Table S8. Seasonal Evaporation, Transpiration and Evapotranspiration (ET) of two ecosystems.

	Growing season in 2016		**Growing season in 2019**	
Unit: [mm season^{-1}]	Grassland	Shrub and grassland	Grassland	Shrub and grassland
Rainfall (Sum)	218.1 mm (*dry*)		292.4 mm (*normal*)	
Evaporation (Sum ± SD)	175.56 ± 96.74	138.58 ± 80.58	220.68 ± 123.47	187.99 ± 109.19
Difference (Shrub − Grassland)	−36.98 ± 26.87		−32.68 ± 25.91	
Transpiration (Sum ± SD)	74.46 ± 29.17	125.53 ± 52.88	74.16 ± 33.63	130.14 ± 75.17
Difference (Shrub − Grassland)	51.07 ± 24.96		55.98 ± 43.01	
ET (Sum ± SD)	250.02 ± 118.70	264.11 ± 119.76	294.84 ± 145.60	318.13 ± 155.14
Difference (Shrub − Grassland)	14.09 ± 21.92		23.30 ± 28.58	

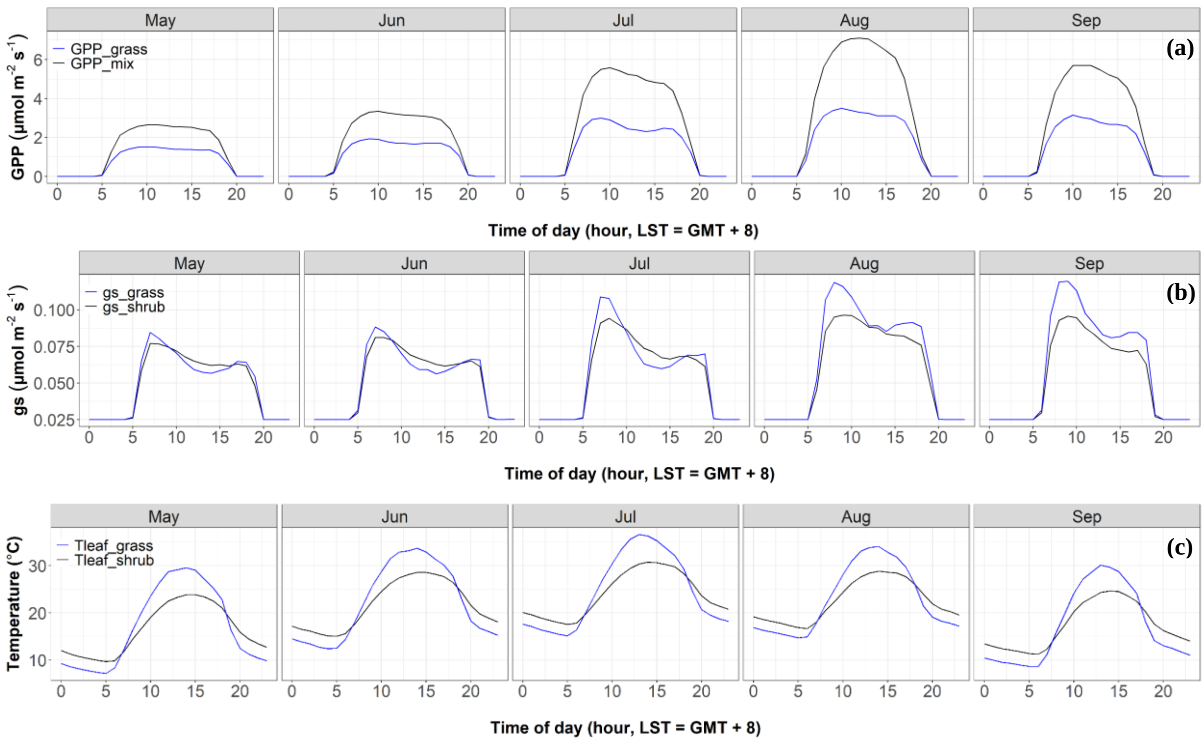

Figure S10. Diurnal courses of simulated (a) Gross Primary Productivity (GPP); (b) stomatal conductance (gs); and (c) leaf temperature (Tleaf) of two ecosystems during May–September in 2016 and 2019.

Table S9. Seasonal simulated Gross Primary Productivity (GPP) of two ecosystems.

	Growing season in 2016		Growing season in 2019	
GPP Unit: [gC m^{-2} $season^{-1}$]	Grassland	Shrub and grassland	Grassland	Shrub and grassland
Rainfall (Sum)	218.1 mm (*dry*)		292.4 mm (*normal*)	
GPP (Sum $\pm$ SD)	183.56 $\pm$ 59.05	323.82 $\pm$ 102.32	196.60 $\pm$ 74.28	372.51 $\pm$ 169.18
Difference (Shrub – Grassland)	150.26 $\pm$ 47.51		175.92 $\pm$ 98.88	

6 Uncertainties in simulating LE and GPP

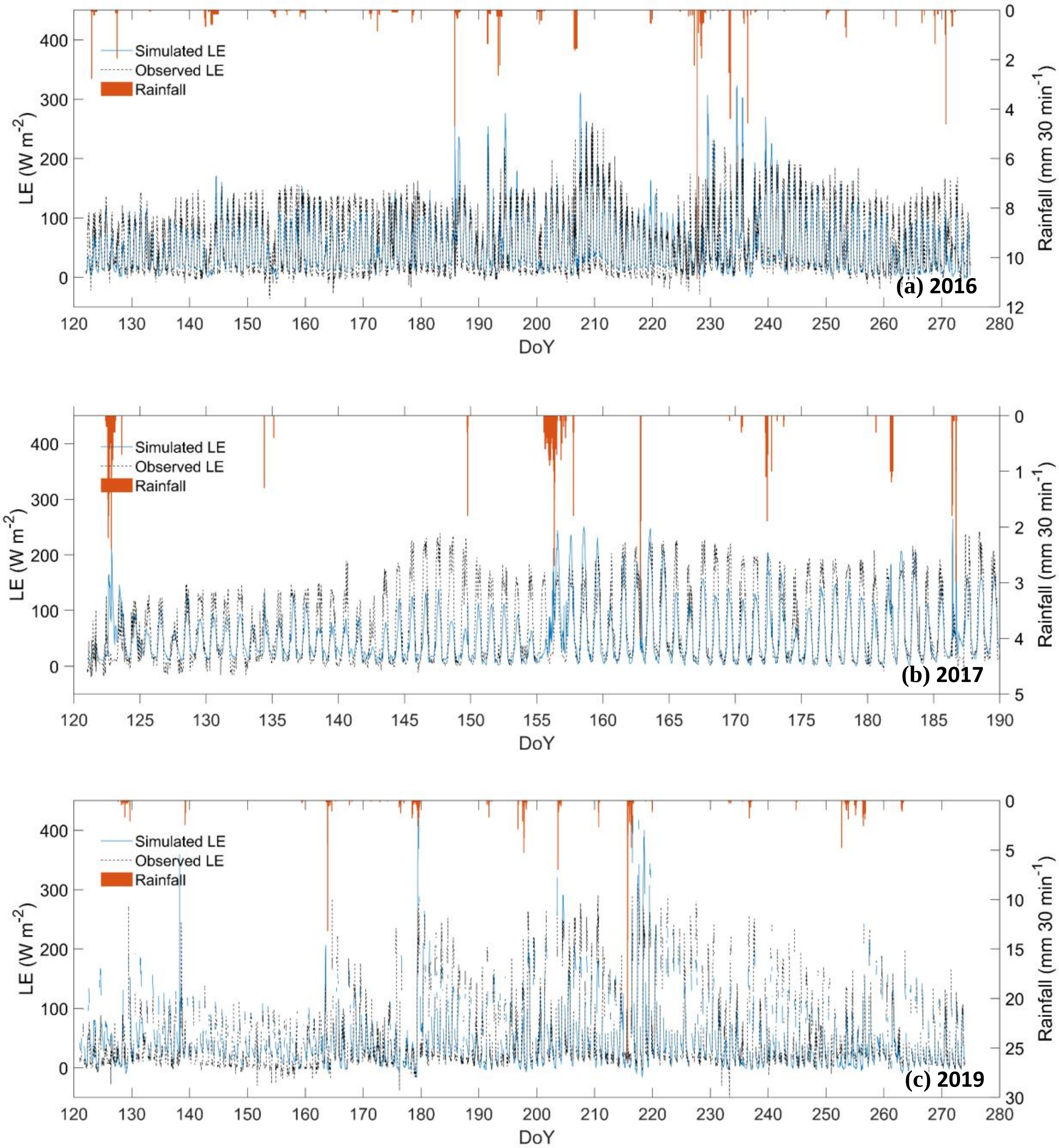

Figure S11. Comparison of the simulated and observed half-hourly values of latent heat flux (LE) of shrubs-grassland ecosystem in (a) 2016, (b) 2017 and (c) 2019.

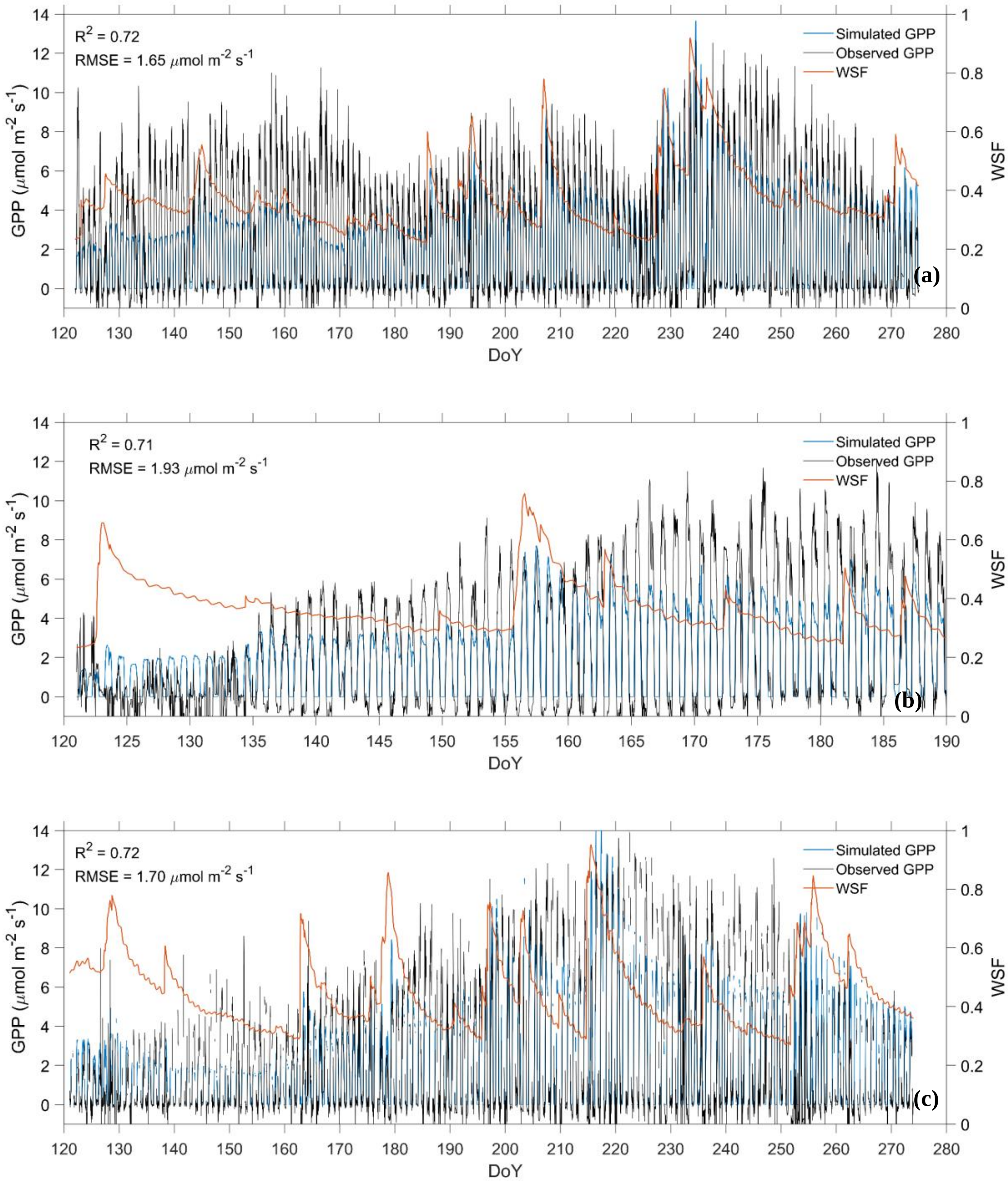

Figure S12. Comparison of the simulated and observed half-hourly values of gross primary productivity (GPP) of the shrubs-grassland ecosystem in (a) 2016, (b) 2017 and (c) 2019.

References

Abouali, M.: MATLAB Implementation of Harmonic ANalysis of Time Series (HANTS), https://www.mathworks.com/matlabcentral/fileexchange/38841-matlab-implementation-of-harmonic-analysis-of-time-series-hants, MATLAB Central File Exchange, 2012.

Abu-Hamdeh, N. H.: Thermal Properties of Soils as affected by Density and Water Content, Biosyst. Eng., 86, 97–102, https://doi.org/10.1016/S1537-5110(03)00112-0, 2003.

Bayat, B., van der Tol, C., Yang, P., and Verhoef, W.: Extending the SCOPE model to combine optical reflectance and soil moisture observations for remote sensing of ecosystem functioning under water stress conditions, Remote Sens. Environ., 221, 286–301, https://doi.org/10.1016/J.RSE.2018.11.021, 2019.

Bennett, W. B., Wang, J., and Bras, R. L.: Estimation of Global Ground Heat Flux, J. Hydrometeorol., 9, 744–759, https://doi.org/10.1175/2008JHM940.1, 2008.

Campolongo, F., Cariboni, J., and Saltelli, A.: An effective screening design for sensitivity analysis of large models, Environ. Model. Softw., 22, 1509–1518, https://doi.org/10.1016/J.ENVSOFT.2006.10.004, 2007.

Collatz, G. J., Ball, J. T., Grivet, C., and Berry, J. A.: Physiological and environmental regulation of stomatal conductance, photosynthesis and transpiration: a model that includes a laminar boundary layer, Agric. For. Meteorol., 54, 107–136, https://doi.org/10.1016/0168-1923(91)90002-8, 1991.

Farquhar, G. D., von Caemmerer, S., and Berry, J. A.: A biochemical model of photosynthetic CO2 assimilation in leaves of C3 species, Planta 1980 1491, 149, 78–90, https://doi.org/10.1007/BF00386231, 1980.

Foken, T.: The energy balance closure problem: an overview, Ecol. Appl., 18, 1351–1367, https://doi.org/10.1890/06-0922.1, 2008.

Gao, Z., Russell, E. S., Missik, J. E. C., Huang, M., Chen, X., Strickland, C. E., Clayton, R., Arntzen, E., Ma, Y., and Liu, H.: A novel approach to evaluate soil heat flux calculation: An analytical review of nine methods, J. Geophys. Res. Atmos., 122, 6934–6949, https://doi.org/10.1002/2017JD027160, 2017.

Gong, J., Jia, X., Zha, T., Wang, B., Kellomäki, S., and Peltola, H.: Modeling the effects of plant-interspace heterogeneity on water-energy balances in a semiarid ecosystem, Agric. For. Meteorol., 221, 189–206, https://doi.org/10.1016/J.AGRFORMET.2016.01.144, 2016.

He, J., Yang, K., Tang, W., Lu, H., Qin, J., Chen, Y., and Li, X.: The first high-resolution meteorological forcing dataset for land process studies over China, Sci. Data 2020 71, 7, 1–11, https://doi.org/10.1038/s41597-020-0369-y, 2020.

Jackson, R. B., Mooney, H. A., and Schulze, E. D.: A global budget for fine root biomass, surface area, and nutrient contents, Proc. Natl. Acad. Sci. U. S. A., 94, 7362–7366, https://doi.org/10.1073/PNAS.94.14.7362, 1997.

Jia, X., Zha, T., Gong, J., Zhang, Y., Wu, B., Qin, S., and Peltola, H.: Multi-scale dynamics and environmental controls on net ecosystem CO2 exchange over a temperate semiarid shrubland, Agric. For. Meteorol., 259, 250–259, https://doi.org/10.1016/J.AGRFORMET.2018.05.009, 2018.

Jiang, L., Liu, H., Peng, Z., Dai, J., Zhao, F., and Chen, Z.: Root system plays an important role in responses of plant to drought in the steppe of China, L. Degrad. Dev., 32, 3498–3506, https://doi.org/10.1002/LDR.3930, 2021.

Lai, Z., Zhang, Y., Liu, J., Wu, B., Qin, S., and Fa, K.: Fine-root distribution, production, decomposition, and effect on soil organic carbon of three revegetation shrub species in northwest China, For. Ecol. Manage., 359, 381–388, https://doi.org/10.1016/J.FORECO.2015.04.025, 2016.

Li, Z., Yu, G., Wen, X., Zhang, L., Ren, C., and Fu, Y.: Energy balance closure at ChinaFLUX sites, Sci. China, Ser. D Earth Sci., 48, 51–62, https://doi.org/10.1360/05ZD0005, 2005.

Liang, M., Smith, N. G., Chen, J., Wu, Y., Guo, Z., Gornish, E. S., and Liang, C.: Shifts in plant composition mediate grazing effects on carbon cycling in grasslands, J. Appl. Ecol., 58, 518–527, https://doi.org/10.1111/1365-2664.13824, 2021.

Montzka, C., Herbst, M., Weihermüller, L., Verhoef, A., and Vereecken, H.: A global data set of soil hydraulic properties and sub-grid variability of soil water retention and hydraulic conductivity curves, Earth Syst. Sci. Data, 9, 529–543, https://doi.org/10.5194/ESSD-9-529-2017, 2017.

Morris, M. D.: Factorial Sampling Plans for Preliminary Computational Experiments, Technometrics, 33, 161, https://doi.org/10.2307/1269043, 1991.

Murray, T. and Verhoef, A.: Moving towards a more mechanistic approach in the determination of soil heat flux from remote measurements: I. A universal approach to calculate thermal inertia, Agric. For. Meteorol., 147, 80–87, https://doi.org/10.1016/J.AGRFORMET.2007.07.004, 2007.

Mwangi, S., Zeng, Y., Montzka, C., Yu, L., and Su, Z.: Assimilation of Cosmic-Ray Neutron Counts for the Estimation of Soil Ice Content on the Eastern Tibetan Plateau, J. Geophys. Res. Atmos., 125, https://doi.org/10.1029/2019JD031529, 2020.

Roerink, G. J., Menenti, M., and Verhoef, W.: Reconstructing cloudfree NDVI composites using Fourier analysis of time series, Int. J. Remote Sens., 21, 1911–1917, https://doi.org/10.1080/014311600209814, 2000.

Tang, S., Jia, X., Guo, J., Chen, Z., Zha, T., Qin, S., and Yang, L.: Measuring and modeling leaf area index for Artemisia ordosica (In Chinese), Chinese J. Ecol., 33, 547–554, https://www.researchgate.net/publication/289227477_Measuring_and_modeling_leaf_area_index_for_Artemisia_ordosica, 2014.

Troufleau, D., Lhomme, J. P., Monteny, B., and Vidal, A.: Sensible heat flux and radiometric surface temperature over sparse Sahelian vegetation. I. An experimental analysis of the kB−1 parameter, J. Hydrol., 188–189, 815–838, https://doi.org/10.1016/S0022-1694(96)03172-1, 1997.

Valayamkunnath, P., Sridhar, V., Zhao, W., and Allen, R. G.: Intercomparison of surface energy fluxes, soil moisture, and evapotranspiration from eddy covariance, large-aperture scintillometer, and modeling across three ecosystems in a semiarid climate, Agric. For. Meteorol., 248, 22–47, https://doi.org/10.1016/J.AGRFORMET.2017.08.025, 2018.

Wallace, J. S. and Verhoef, A.: Interactions in mixed-plant communities: light, water and carbon dioxide. In: Marshall, Roberts (Eds.). Leaf Development and Canopy Growth. , in: Sheffield Biological Science Series, Sheffield Academic Press, 204–250, 2000.

Wang, Y., Zeng, Y., Yu, L., Yang, P., Van der Tol, C., Yu, Q., Lü, X., Cai, H., and Su, Z.: Integrated modeling of canopy photosynthesis, fluorescence, and the transfer of energy, mass, and momentum in the soil-plant-Atmosphere continuum (STEMMUS-SCOPE v1.0.0), Geosci. Model Dev., 14, 1379–1407, https://doi.org/10.5194/gmd-14-1379-2021, 2021.

Wei, Y., Wang, Y., Han, J., Cai, M., Zhu, K., and Wang, Q.: Analysis of water retention characteristics of oil-polluted earthy materials with different textures based on van Genuchten model, J. Soils Sediments, 19, 373–380, https://doi.org/10.1007/S11368-018-2026-Z, 2019.

Zeng, Y., Su, Z., Wan, L., and Wen, J.: A simulation analysis of the advective effect on evaporation using a two-phase heat and mass flow model, Water Resour. Res., 47, https://doi.org/10.1029/2011WR010701, 2011a.

Zeng, Y., Su, Z., Wan, L., and Wen, J.: Numerical analysis of air-water-heat flow in unsaturated soil: Is it necessary to consider airflow in land surface models?, J. Geophys. Res. Atmos., 116, D20107, https://doi.org/10.1029/2011JD015835, 2011b.